Supporting Information to

Universal Approach to Fabricating Graphene-Supported Single-Atom Catalysts from Doped ZnO Solid Solution

Jiashen Meng, Jiantao Li, Jinshuai Liu, Xingcai Zhang, Gengping Jiang,* Lu Ma, Zhi-Yi Hu, Shibo Xi, Yunlong Zhao, Mengyu Yan, Peiyao Wang, Xiong Liu, Qidong Li, Jefferson Zhe Liu, Tianpin Wu, and Liqiang Mai**

[*]E-mail: mlq518@whut.edu.cn; gengpingjiang@wust.edu.cn; xingcai@mit.edu

Table of Contents

Experimental Procedures

Supplementary Figures

Supplementary Tables

References

Experimental Procedures

Synthesis of M-N-Gr. All the chemicals used were analytical grade without further treatment. First, various doped ZnO nanoparticles were preferentially synthesized as template precursors. In a typical synthesis, zinc acetate (32 mmol) was dissolved in 100 ml of ethanol by stirring at 65 °C for 1 h. 1 mmol of metal nitrate (e.g., cobalt nitrate hexahydrate, copper nitrate hydrate, nickel nitrate hexahydrate, ferrous nitrate hexahydrate) was dissolved in 20 ml of ethanol and then poured into the former zinc acetate solution. 40 mmol of citric acid was dissolved in 50 ml of ethanol and was then added dropwise to the above-mixed solution to produce a sol. The sol was stirred for 1 h and baked in an oven at 70 °C for 24 h to obtain a gel. The gel was calcined at 500~600 °C for 6 h in air to obtain $Zn_{0.97}M_{0.03}O$ nanoparticles at a heating rate of 5 °C min^{-1}. Second, the as-prepared $Zn_{0.97}M_{0.03}O$ nanoparticles and 2-methylimidazole (2-MIM) were both treated at 140 °C for 6 h under a low-pressure (~50 Pa) condition in one system. The mass ratio of $Zn_{0.97}M_{0.03}O$ nanoparticles and 2-methylimidazole is about 1:20. After low-pressure vapor superassembly, a thin coating layer of M-doped ZIF was formed on the surfaces of $Zn_{0.97}M_{0.03}O$ nanoparticles. Subsequently, the $Zn_{0.97}M_{0.03}O$@ZIF nanoparticles were calcined in N_2 at 650 °C for 3 h, forming $Zn_{0.97}M_{0.03}O$@M-N-Gr nanoparticles. Then, the $Zn_{0.97}M_{0.03}O$@M-N-Gr nanoparticles were immersed into hydrochloric acid aqueous solution (15 wt%) under ultrasonic condition for 12 h to remove the inner $Zn_{0.97}M_{0.03}O$ cores. Finally, after treated in N_2 at 800 °C for 2 h, the M-N-Gr hollow structures were obtained. In addition, when increasing the addition content of cobalt nitrate hexahydrate, the $Zn_{0.95}Co_{0.05}O$ nanoparticles were synthesized and then the Co-N-Gr hollow structure with high mass loading of Co atoms (Co-N-Gr-H) can be also obtained via the above procedures. When treated without the addition of doped M, the N-Gr hollow structure can be obtained.

Safety Statement. No unexpected or unusually high safety hazards were encountered.

Characterizations. The crystallographic characteristics of the final products were measured using a Bruker D8 Discover X-ray diffractometer equipped with a Cu Kα radiation source. SEM images were collected using a JEOL-7100F scanning electron

microscope, and TEM images were performed on a JEM-2100F. HAADF-STEM and EDX were performed on a Titan Themis 60-300 ‘‘cubed’’ microscope fitted with aberration-correctors for the imaging lens and the probe forming lens, Super-X EDX system, operated at 300 kV. UV-Vis spectra were obtained using a Lambda 750 S system. Raman spectra were obtained using a Renishaw INVIA micro-Raman spectroscopy system. The BET surface area was calculated from nitrogen adsorption isotherms collected at 77 K using a Tristar-3020 instrument. The electron paramagnetic resonance (EPR) measurement was conducted with a Bruker EMX Plus spectrometer using an X band (9.78 GHz) at room temperature. XPS and UPS measurements were conducted using an ESCALAB 250Xi instrument. The XAS measurement at Fe, Co, Ni and Cu K-edge was performed at the Advanced Photon Source (APS) on the bending-magnet beamline 9-BM-B with electron energy of 7 GeV and average current of 100 mA. The radiation was monochromatized by a Si (111) double-crystal monochromator. Harmonic rejection was accomplished with Harmonic rejection mirror. All spectra were collected in transmission mode. XAS data reduction and analysis were processed by Athena software.

Electrocatalysis measurements. For the ORR, the electrocatalytic activities of catalysts toward the ORR were measured in O_2-saturated 0.1 M KOH aqueous solution using a Pt wire counter electrode, a saturated Ag/AgCl reference electrode, and a working electrode. An ink of the catalyst was prepared by mixing 8 mg of catalyst powder and 2 mg of Vulcan XC72R (VXC72R) with 50 μL of 5 wt% Nafion solution, 200 μL of deionized water, and 750 μL of isopropanol, and placed the resulting mixture in an ultrasonic bath. Cyclic voltammograms at a sweep rate of 5 $mV \cdot s^{-1}$ were recorded. LSV was performed in O_2-saturated 0.1 M KOH. ORR polarization curves were recorded at a scan rate of 5 $mV \cdot s^{-1}$ under various electrode rotation rates (400, 625, 900, 1225, and 1600 rpm). The Pt ring potential was set at 0.5 V versus Ag/AgCl to monitor the formation of peroxide species. All the potentials were converted to the RHE potential scale.

Before each measurement, the 0.1 M KOH electrolyte was bubbled with O_2 for more than 30 min. RRDE measurements were performed at 1600 rpm using a CHI 760 E electrochemical workstation equipped with an RRDE-E7R9 rotator (Pine Co., Ltd.).

The ORR kinetics were analyzed using the Koutecky-Levich (K-L) equation

$$\frac{1}{i}=\frac{1}{i_k}+\frac{1}{i_d}=-\frac{1}{nFAkC^0}-\frac{1}{0.62nFAD_{O_2}^{2/3}\upsilon^{-1/6}C^0\omega^{1/2}} \qquad (1)$$

where i, i_k, and i_d correspond to the measured, kinetic, and diffusion-limiting currents, respectively; n is the overall transferred electron number; F is the Faraday constant; A is the geometric electrode area (cm^2); *k* is the rate constant for oxygen reduction; C^0 is the saturated concentration of oxygen in 0.1 M KOH; D_{O_2} is the diffusion coefficient of oxygen; υ is the kinetic viscosity of the solution; and ω is the rotation rate ($rad\cdot s^{-1}$) of the electrode. Further, the percentage of peroxide species (HO_2^-) with respect to the total generated oxygen reduction products and the electron reduction number (*n*) were calculated as

$$HO_2^- = 200\frac{I_r/N}{I_d+I_r/N} \qquad (2)$$

$$n = 4\frac{I_d}{I_d+I_r/N} \qquad (3)$$

where I_d is the disk current, I_r is the ring current, and N is the current collection efficiency (0.37) of the RRDE.

All potentials were calibrated with respect to the RHE scale according to the Nernst equation ($E_{RHE} = E_{Ag/AgCl} + 0.059*pH + 0.210$).

Computation details. DFT calculation studies for ORR intermediates were taken using the Vienna Ab initio simulation package (VASP).[S1] The spin-polarized Perdew-Burke-Ernzerhof (PBE) functional and the projector augmented wave (PAW) method were chosen to describe the exchange-correlation energy and electron-ionic cores interaction.[S2-S4] The convergent criterion of electronic structure calculation and geometry optimization was set to be 10^{-5} eV and 0.01 eV $Å^{-1}$, respectively. The plane-

wave basis was utilized with a cut-off at 550 eV in conjuction with a Monkhorst-Pack k-point grid of 3 × 3 × 1. The Gaussian smearing of 0.2 eV for VASP calculation were employed for all electronic structure calculation and geometry optimization. Through the test, the VDW correction of zero damping Grimme-D3 scheme was found to better describe the adsorption of molecules onto the M-N substance, and incorporated into the DFT calculation.[S5] To avoid the spurious interaction between the adjacent layers, a 15 Å spacing of vacuum was added in Z-direction as an adjustment between computational accuracy and cost. [S6,S7] Both the supercell and geometry structure of pristine M-N-Gr sheet were optimized and only the geometry optimization results were applied for the following intermediates stages. The Hubbard parameters $U_{eff} = U - J$ for the d orbitals was taken as 6.5 for Fe atoms, 5.3 for Co, and 6.7 for Ni, respectively,[S8] except for 4.0 of Cu from the semi-empirical work.[S9] However, the same Zero Point Energies (ZPE) and entropy contributions for different doping atoms were employed for each stage, as tabulated in Table S5.[S10] The total free energies of intermediates were calculated based on the equation: $G = E + ZPE - TS$.

The four-electron ORR reaction pathway was investigated in the present article. The whole four-electron electrocatalytic pathway was usually divided into following five individual steps: [S11]

(i) $* + O_2 \rightarrow *OO$

(ii) $*OO + H_2O + e^- \rightarrow *OOH + OH^-$

(iii) $*OOH + e^- \rightarrow *O + OH^-$

(iv) $*O + H_2O + e^- \rightarrow *OH + OH^-$

(v) $*OH + e^- \rightarrow * + OH^-$

where (*) denotes the catalytic site to be bound by oxygen gas. Except for the first step of oxygen adsorption, each step in (ii)-(v) involves an electron-proton transfer.

The reaction free energy diagram of ORR in the main text was calculated based on the computational hydrogen electrode (CHE) mode.[S12] Taking the "$*OOH + H^+ + e- \rightarrow H_2O + *O$" process for example, the free energy formula with an applied potential U can be expressed as the following equation:

$$\Delta G = G(H_2O) + G(*O) - G(*OOH) - G(H^+ + e^-) - eU$$

Equivalently,

$$\Delta G = G(H_2O) + G(*O) - G(*OOH) - G(1/2H_2(g)) - eU$$

Where the asterisk symbol denoted the graphene basal plane doped with the different metal atom; "*O" and "*OOH" indicated the binding of an oxygen atoms or "OOH" group onto the M-N-Gr. According to the "CRC Handbook of Chemistry and Physics", the free energy of "H_2O", "O_2", and "H_2" molecules in the ORR process are –14.21 eV, –9.702 eV, and –6.894 eV, respectively. Moreover, the equilibrium metal-oxygen distances of the different metal dopants were listed in Supplementary Table S6.

Supplementary Figures

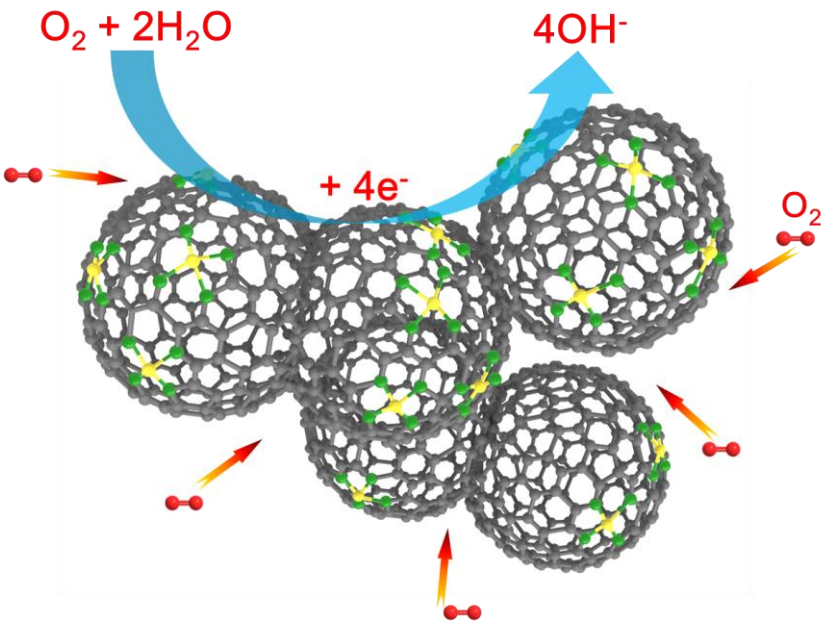

Figure S1. Schematic illustration of single metal atoms anchored in hollow nitrogen-doped graphene frameworks for ORR. This architecture can provide high electrocatalytic activity, high electronic conductivity, efficient O_2 diffusion and fast mass transport and robust structure for ORR.

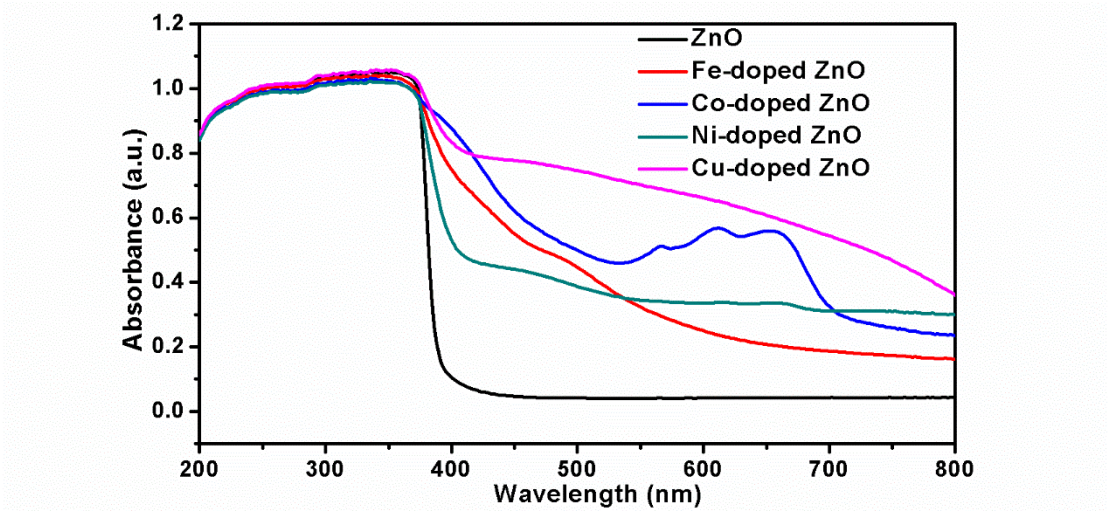

Figure S2. UV-Vis spectra of pure ZnO and various doped ZnO samples.

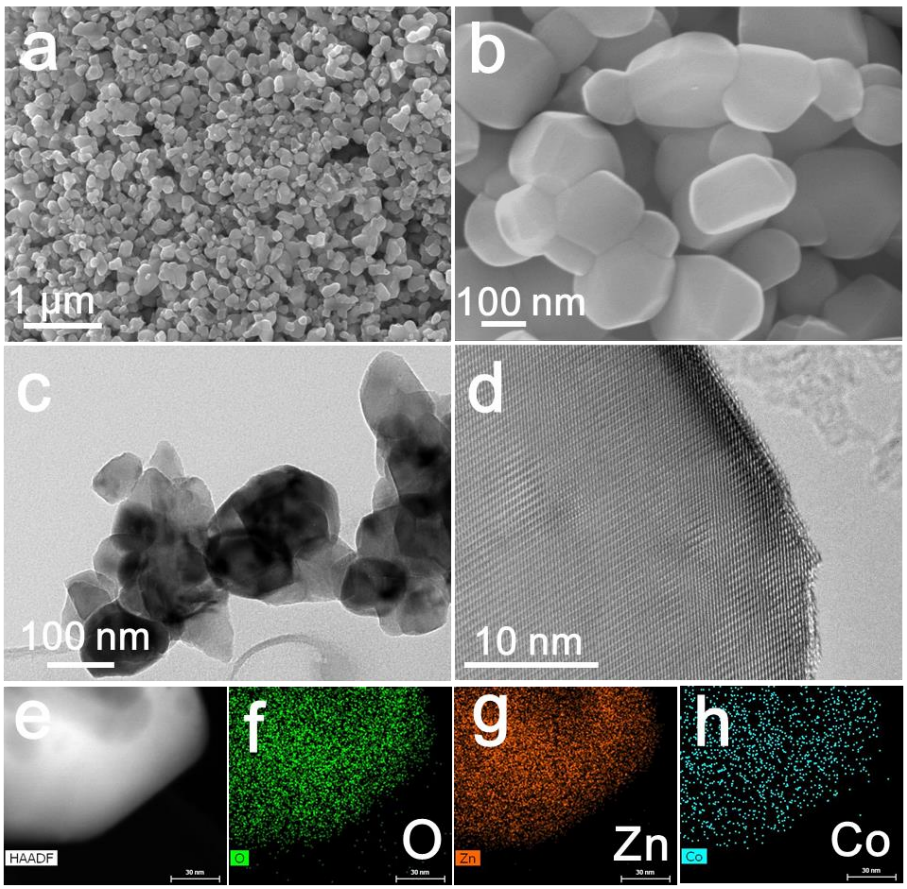

Figure S3. Characterizations of Co-doped ZnO nanoparticles. (**a, b**) SEM images. (**c**) TEM image. (**d**) HRTEM image. (**e-h**) HAADF-STEM image and corresponding EDS elemental maps for O, Zn and Co.

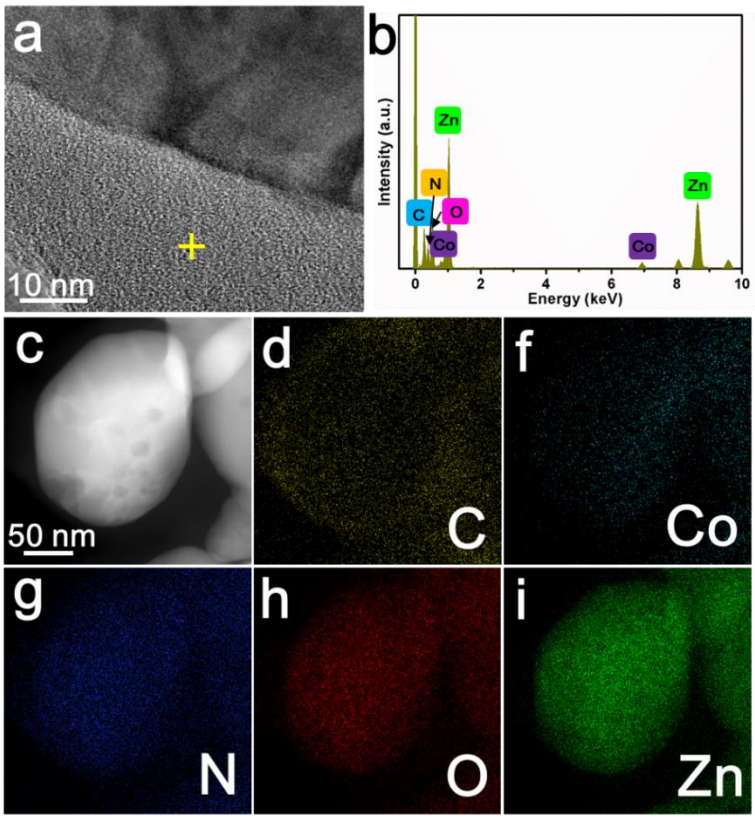

Figure S4. Structural characterizations of Co-doped ZnO@ZIF nanoparticles. (**a**) HRTEM image. (**b**) EDX spectrum. (**c-i**) HAADF-STEM image and the corresponding EDS elemental maps of Co-doped ZnO@ZIF nanoparticles for C, N, O, Zn and Co elements.

Figure S5. Yield evaluation of Co-N-Gr product from Co-doped ZnO templates.

Digital photo shows 0.8 g of the obtained Co-N-Gr product after one time synthesis.

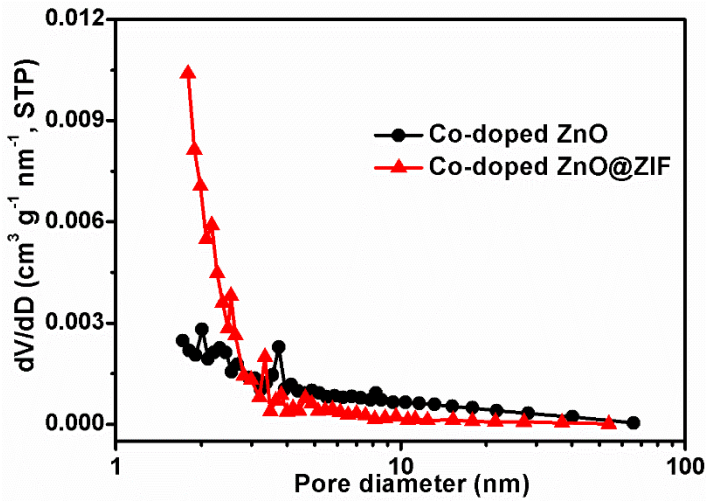

Figure S6. The pore distribution of Co-doped ZnO and Co-doped ZnO@ZIF nanoparticles.

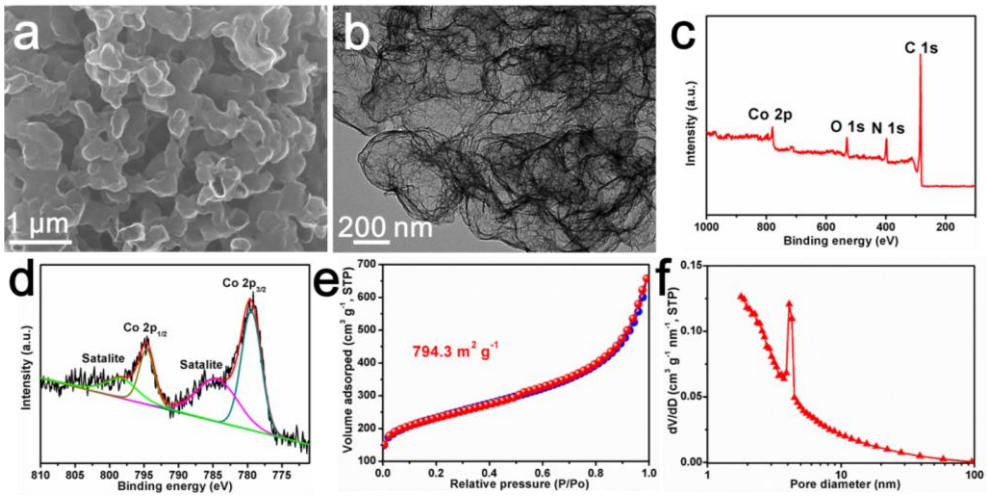

Figure S7. Characterizations of Co-N-Gr sample. (**a**) SEM image. (**b**) TEM image. (**c**) XPS spectrum. (**d**) High-resolution Co 2p XPS spectrum. (**e, f**) N_2 adsorption-desorption isotherms and the pore size distribution.

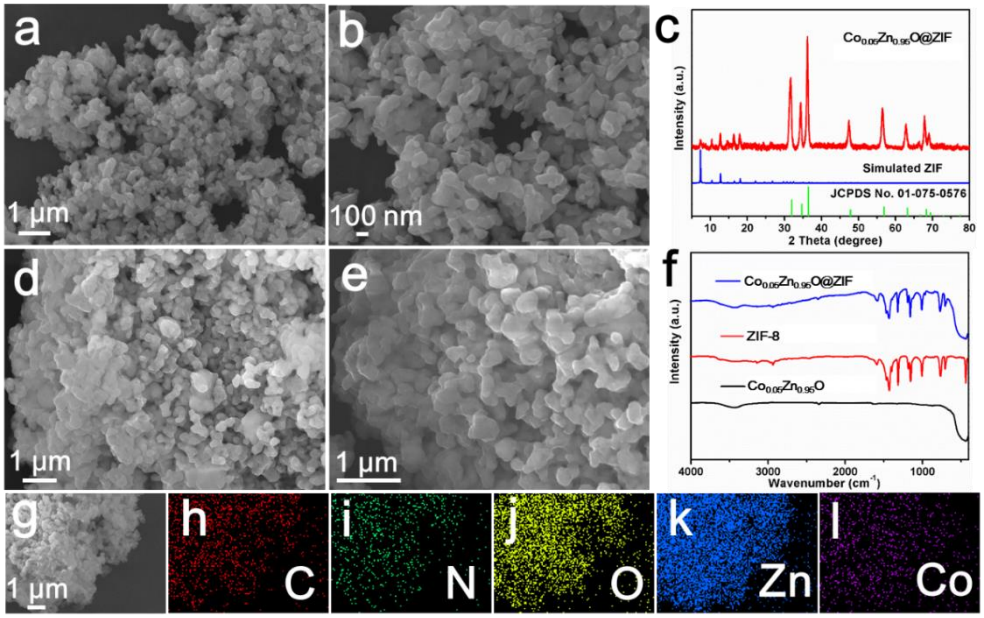

Figure S8. Characterizations of $Co_{0.05}Zn_{0.95}O$ nanoparticles and $Co_{0.05}Zn_{0.95}O$@ZIF nanoparticles. (**a, b**) SEM images of $Co_{0.05}Zn_{0.95}O$ nanoparticles. (**c**) XRD pattern of $Co_{0.05}Zn_{0.95}O$@ZIF nanoparticles. (**d, e**) SEM images of $Co_{0.05}Zn_{0.95}O$@ZIF nanoparticles. (**f**) FTIR spectra of $Co_{0.05}Zn_{0.95}O$ nanoparticles, ZIF-8 and $Co_{0.05}Zn_{0.95}O$@ZIF nanoparticles. (**g-l**) SEM image of $Co_{0.05}Zn_{0.95}O$@ZIF nanoparticles and corresponding EDS elemental maps of C, N, O, Zn and Co.

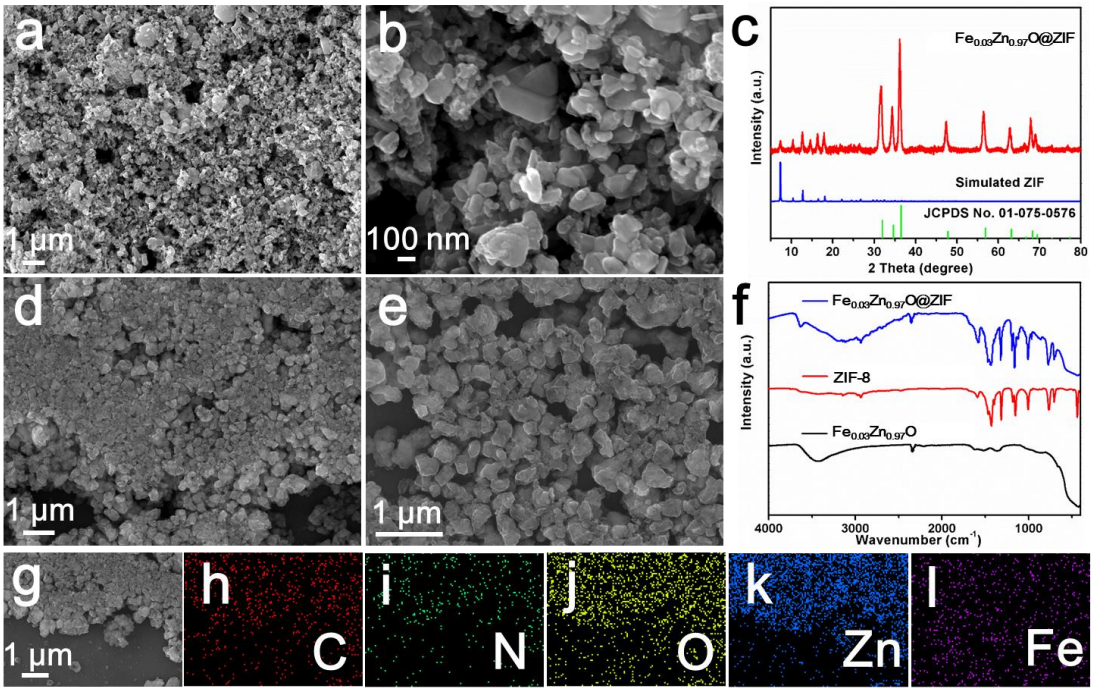

Figure S9. Characterizations of $Fe_{0.03}Zn_{0.97}O$ nanoparticles and $Fe_{0.03}Zn_{0.97}O$@ZIF nanoparticles. (**a, b**) SEM images of $Fe_{0.03}Zn_{0.97}O$ nanoparticles. (**c**) XRD pattern of $Fe_{0.03}Zn_{0.97}O$@ZIF nanoparticles. (**d, e**) SEM images of $Fe_{0.03}Zn_{0.97}O$@ZIF nanoparticles. (**f**) FTIR spectra of $Fe_{0.03}Zn_{0.97}O$ nanoparticles, ZIF-8 and $Fe_{0.03}Zn_{0.97}O$@ZIF nanoparticles. (**g-l**) SEM image of $Fe_{0.03}Zn_{0.97}O$@ZIF nanoparticles and corresponding EDS elemental maps of C, N, O, Zn and Fe.

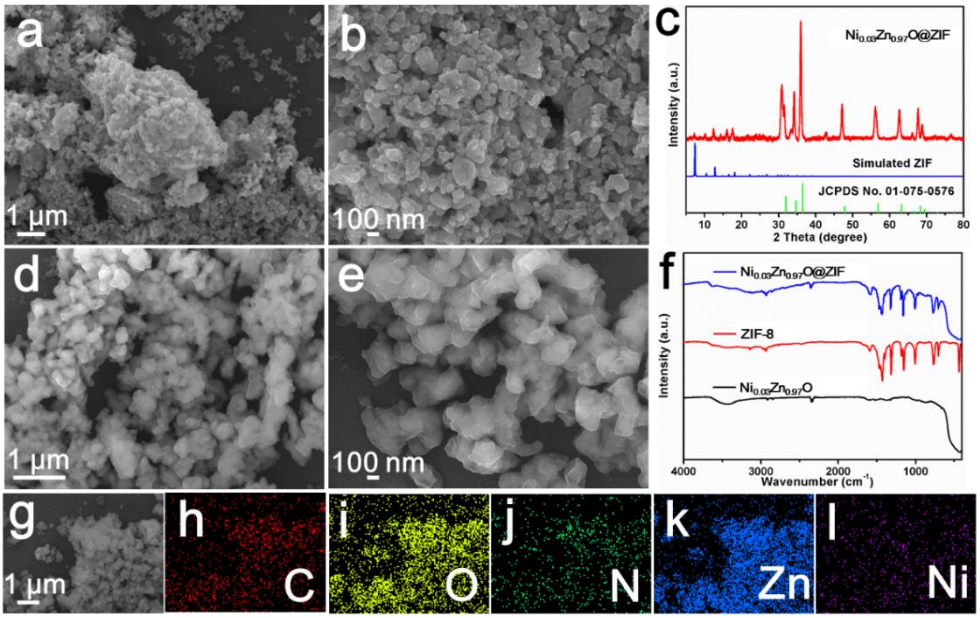

Figure S10. Characterizations of $Ni_{0.03}Zn_{0.97}O$ nanoparticles and $Ni_{0.03}Zn_{0.97}O$@ZIF nanoparticles. (**a, b**) SEM images of $Ni_{0.03}Zn_{0.97}O$ nanoparticles. (**c**) XRD pattern of $Ni_{0.03}Zn_{0.97}O$@ZIF nanoparticles. (**d, e**) SEM images of $Ni_{0.03}Zn_{0.97}O$@ZIF nanoparticles. (**f**) FTIR spectra of $Ni_{0.03}Zn_{0.97}O$ nanoparticles, ZIF-8 and $Ni_{0.03}Zn_{0.97}O$@ZIF nanoparticles. (**g-l**) SEM image of $Ni_{0.03}Zn_{0.97}O$@ZIF nanoparticles and corresponding EDS elemental maps of C, N, O, Zn and Ni.

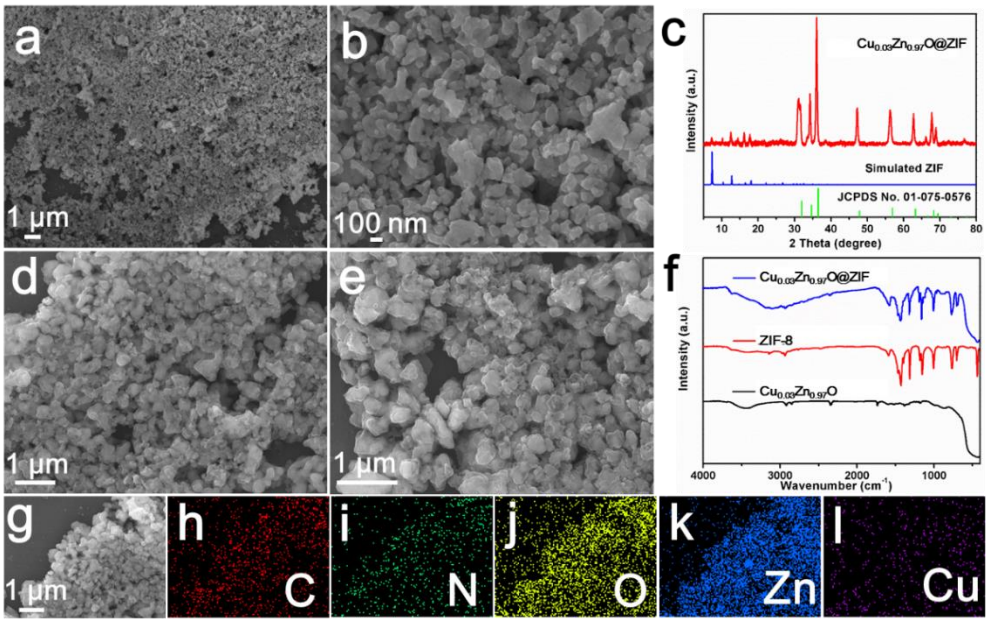

Figure S11. Characterizations of $Cu_{0.03}Zn_{0.97}O$ nanoparticles and $Cu_{0.03}Zn_{0.97}O$@ZIF nanoparticles. (**a, b**) SEM images of $Cu_{0.03}Zn_{0.97}O$ nanoparticles. (**c**) XRD pattern of $Cu_{0.03}Zn_{0.97}O$@ZIF nanoparticles. (**d, e**) SEM images of $Cu_{0.03}Zn_{0.97}O$@ZIF nanoparticles. (**f**) FTIR spectra of $Cu_{0.03}Zn_{0.97}O$ nanoparticles, ZIF-8 and $Cu_{0.03}Zn_{0.97}O$@ZIF nanoparticles. (**g-l**) SEM image of $Cu_{0.03}Zn_{0.97}O$@ZIF nanoparticles and corresponding EDS elemental maps of C, N, O, Zn and Cu.

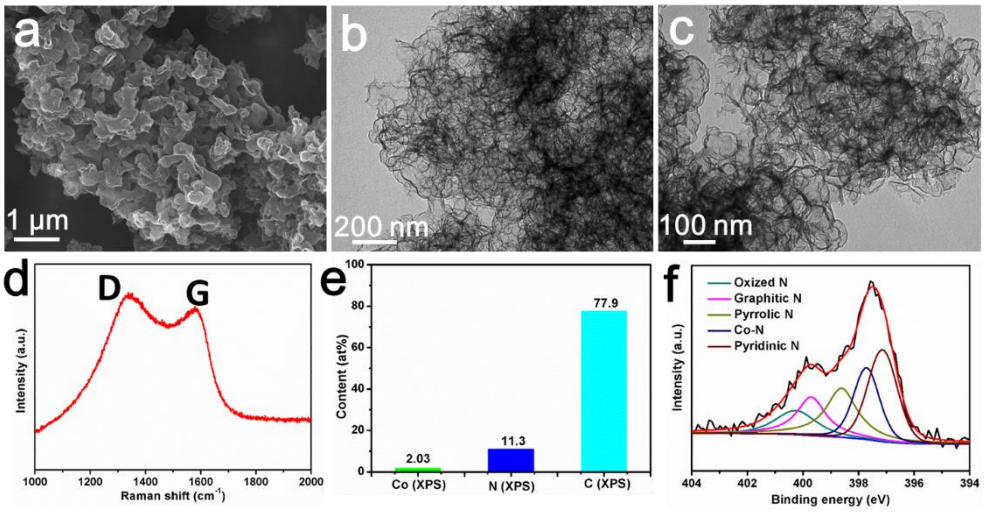

Figure S12. Characterizations of the Co-N-Gr-H sample. (**a**) SEM imags. (**b, c**) TEM images and SAED pattern (inset). (**d**) Raman spectrum. (**e**) Elemental content obtained from XPS measurement. (**f**) High-resolution N 1s XPS spectrum, which was divided into five Voigt-type line-shaped peaks.

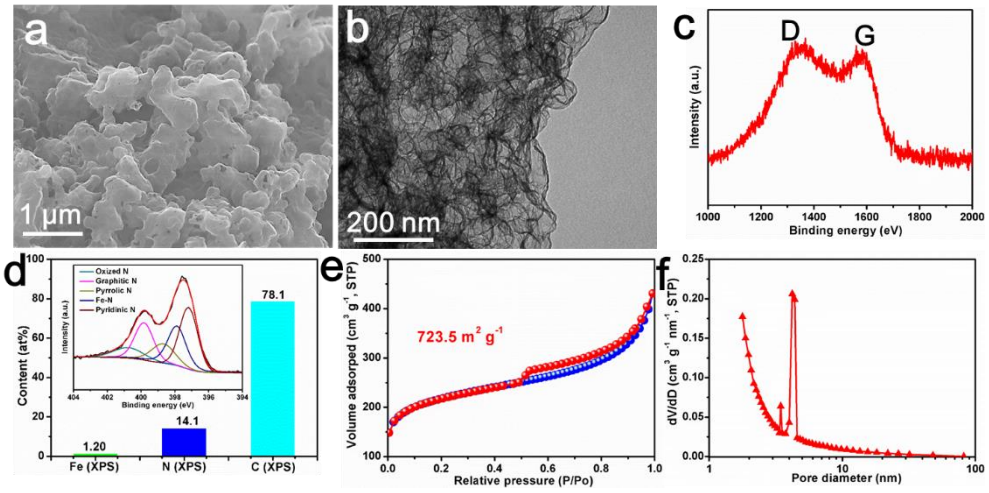

Figure S13. Characterizations of the Fe-N-Gr sample. (**a**) SEM image. (**b**) TEM image. (**c**) Raman spectrum. (**d**) Elemental content obtained from XPS measurement and high-resolution N1s XPS spectrum (inset) divided into five Voigt-type line-shaped peaks. (**e, f**) N_2 adsorption-desorption isotherms and the pore size distribution.

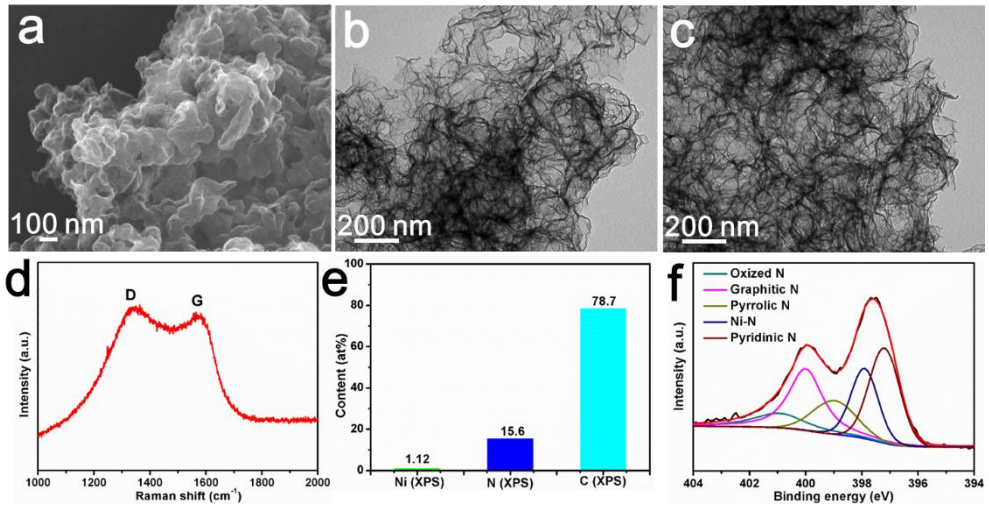

Figure S14. Characterizations of the Ni-N-Gr sample. (**a**) SEM image. (**b, c**) TEM images. (**d**) Raman spectrum. (**e**) Elemental content obtained from XPS measurement. (**f**) High-resolution N1s XPS spectrum divided into five Voigt-type line-shaped peaks.

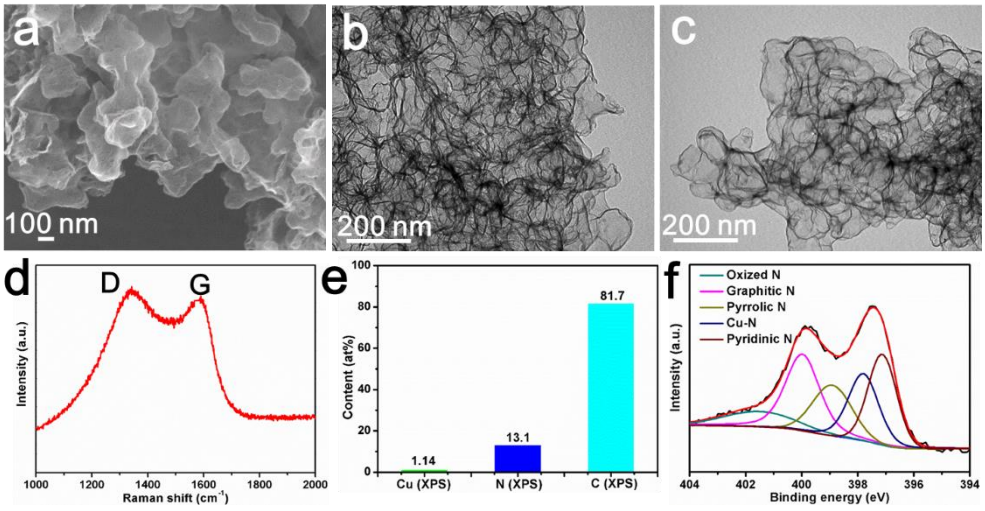

Figure S15. Characterizations of the Cu-N-Gr sample. (**a**) SEM image. (**b, c**) TEM images. (**d**) Raman spectrum. (**e**) Elemental content obtained from XPS measurement. (**f**) High-resolution N1s XPS spectrum divided into five Voigt-type line-shaped peaks.

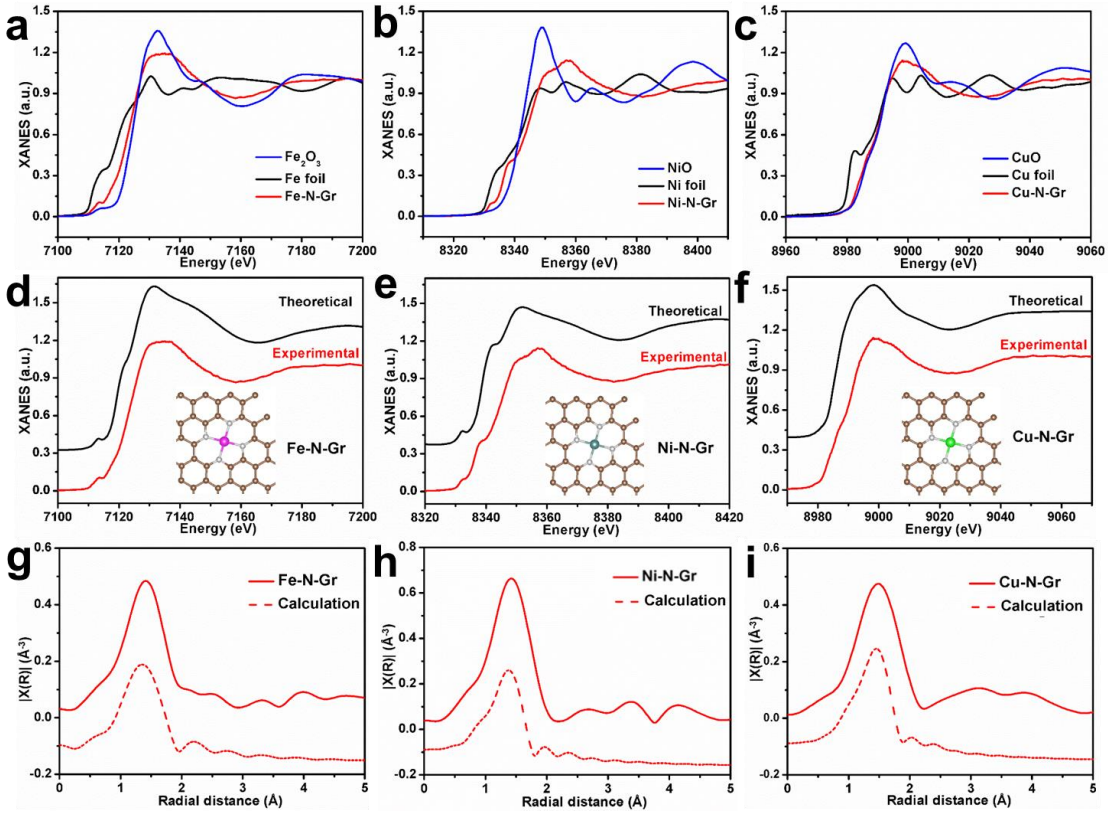

Figure S16. Structural characterizations of Fe-N-Gr, Ni-N-Gr and Cu-N-Gr. (**a**) Fe K-edge XANES spectra of Fe-N-Gr, Fe foil and Fe_2O_3. (**b**) Ni K-edge XANES spectra of Ni-N-Gr, Ni foil and NiO. (**c**) Cu K-edge XANES spectra of Cu-N-Gr, Cu foil and CuO. (**d-f**) Comparison of the experimental K-edge XANES spectra (red lines) and the corresponding theoretical spectra (black lines). Insets of (**d-f**) are the structure of the metal site in M-N-Gr. (**g-i**) Comparison of the experimental K-edge EXAFS spectra and the corresponding theoretical spectra (red dotted lines).

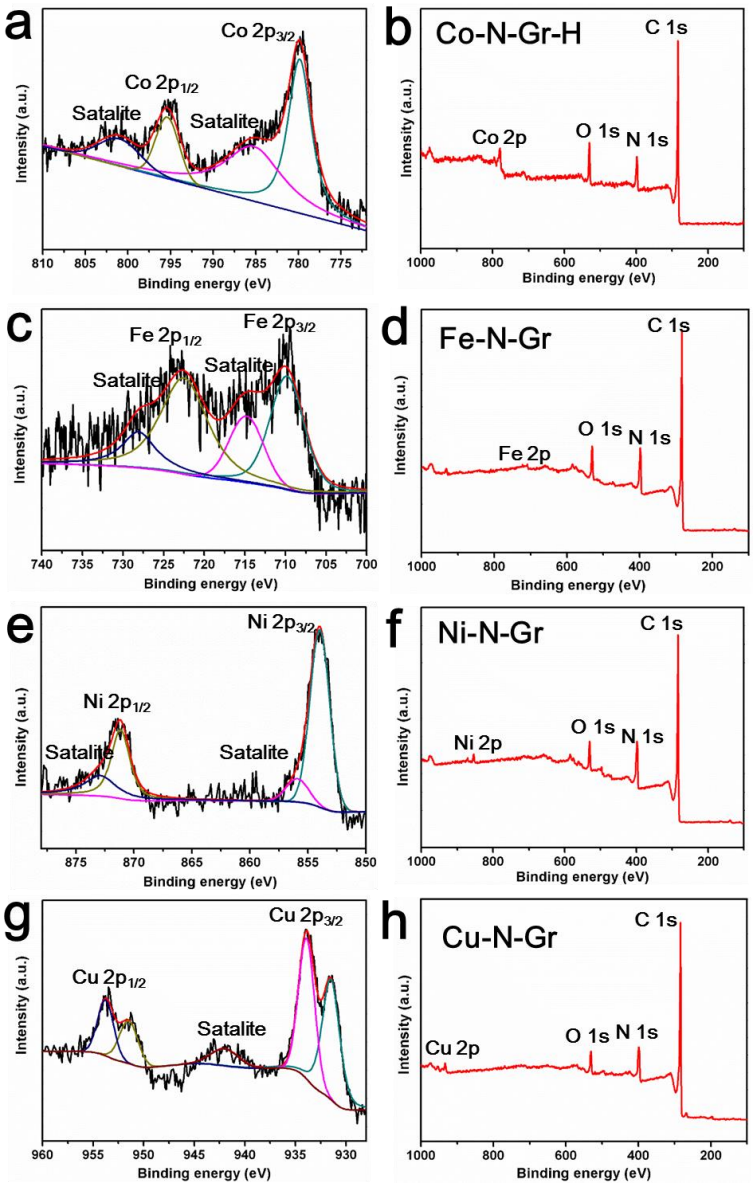

Figure S17. XPS spectra of Co-N-Gr-H, Fe-N-Gr, Ni-N-Gr and Cu-N-Gr. (a, b) High-resolution Co 2p XPS spectrum and full XPS spectrum of Co-N-Gr-H. (c, d) High-resolution Fe 2p XPS spectrum and full XPS spectrum of Fe-N-Gr. (e, f) High-resolution Ni 2p XPS spectrum and full XPS spectrum of Ni-N-Gr. (g, h) High-resolution Cu 2p XPS spectrum and full XPS spectrum of Cu-N-Gr.

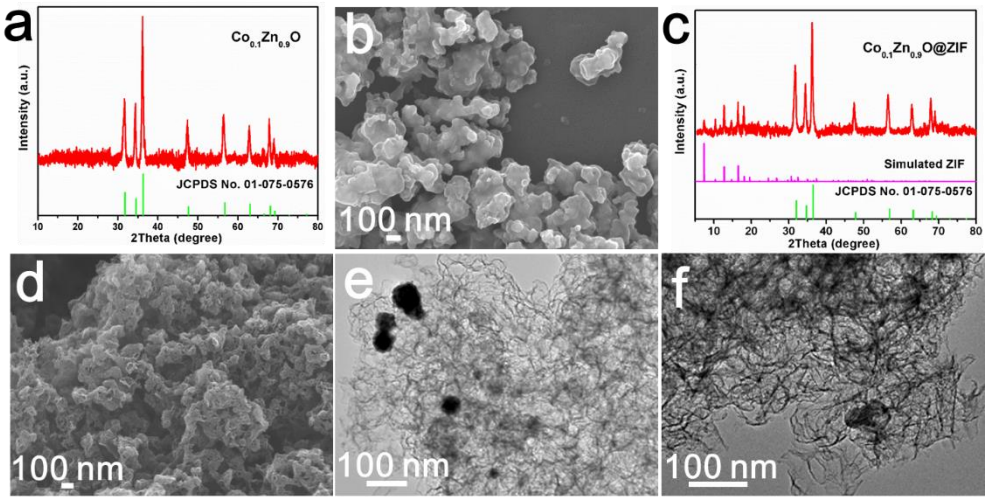

Figure S18. Characterizations of $Co_{0.1}Zn_{0.9}O$, $Co_{0.1}Zn_{0.9}O$@ZIF and the derived product. (**a**) XRD pattern of $Co_{0.1}Zn_{0.9}O$ nanoparticles. SEM image (**b**) and XRD pattern (c) of $Co_{0.1}Zn_{0.9}O$@ZIF nanoparticles. SEM image (**d**) and TEM images (**e, f**) of the derived product.

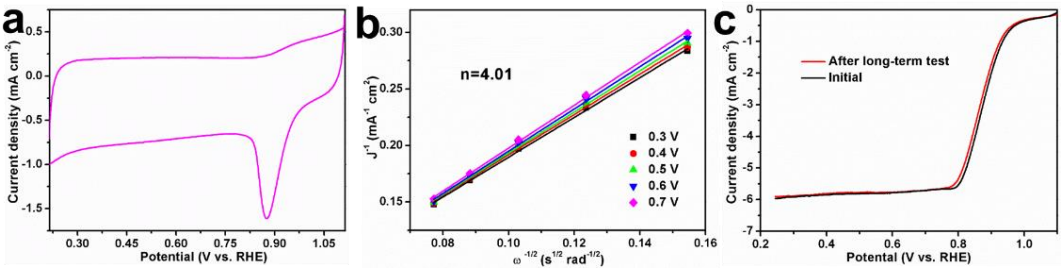

Figure S19. ORR electrocatalytic performances of Fe-N-Gr. (**a**) CV curve of Fe-N-Gr in 0.1 M KOH at 5 $mV \cdot s^{-1}$. (**b**) K-L plots of Fe-N-Gr at different rotating speeds. (**c**) LSV curves of Fe-N-Gr in O_2-saturated 0.1 M KOH at 1225 rpm and a scan rate of 5 $mV \cdot s^{-1}$ before and after long-term test.

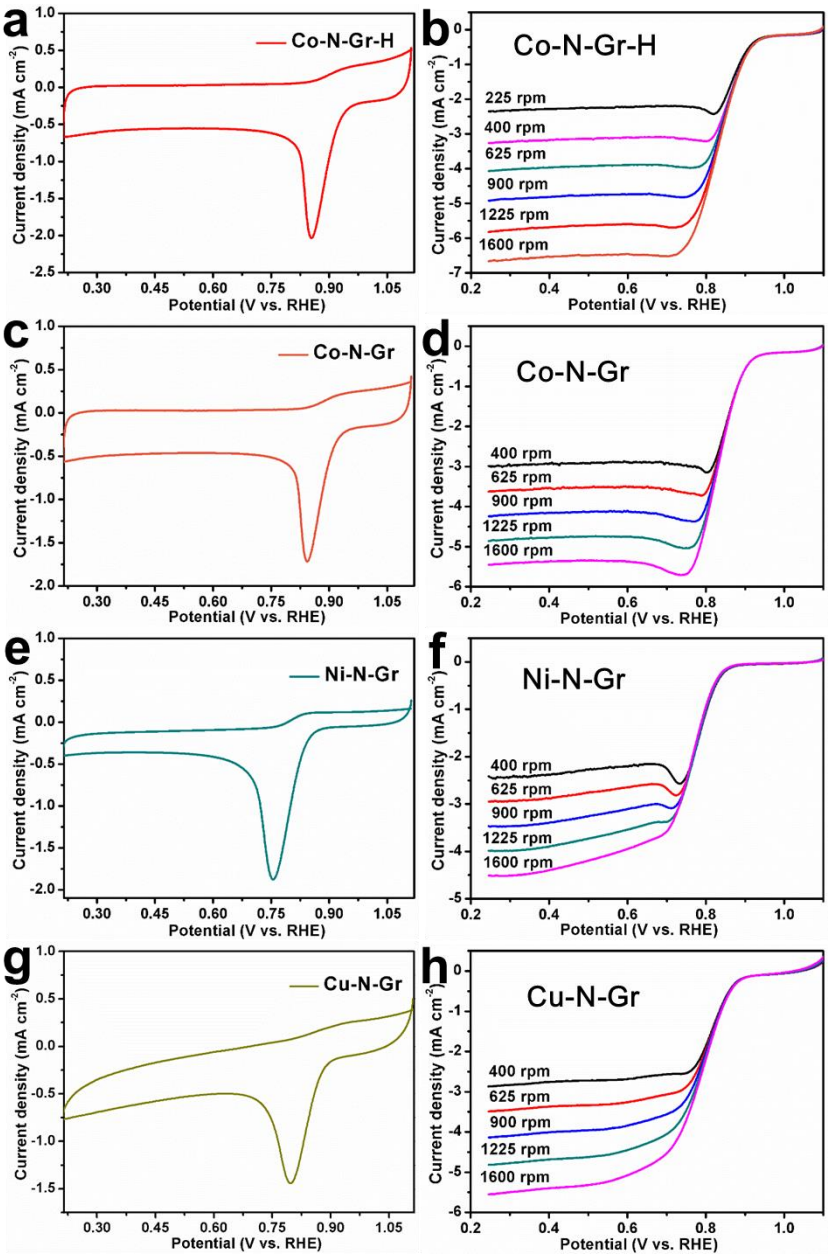

Figure S20. ORR electrocatalytic performances of M-N-Gr samples. (a) CV curve of Co-N-Gr-H in 0.1 M KOH at 5 $mV \cdot s^{-1}$. (b) LSV curves of Co-N-Gr-H in O_2-saturated 0.1 M KOH at 5 $mV \cdot s^{-1}$ and different rotation rates. (c) CV curve of Co-N-Gr in 0.1 M KOH at 5 $mV \cdot s^{-1}$. (d) LSV curves of Co-N-Gr in O_2-saturated 0.1 M KOH at 5 $mV \cdot s^{-1}$ and different rotation rates. (e) CV curve of Ni-N-Gr in 0.1 M KOH at 5 $mV \cdot s^{-1}$. (f) LSV curves of Ni-N-Gr in O_2-saturated 0.1 M KOH at 5 $mV \cdot s^{-1}$ and different rotation rates. (g) CV curve of Cu-N-Gr in 0.1 M KOH at 5 $mV \cdot s^{-1}$. (h) LSV curves of Cu-N-Gr in O_2-saturated 0.1 M KOH at 5 $mV \cdot s^{-1}$ and different rotation rates.

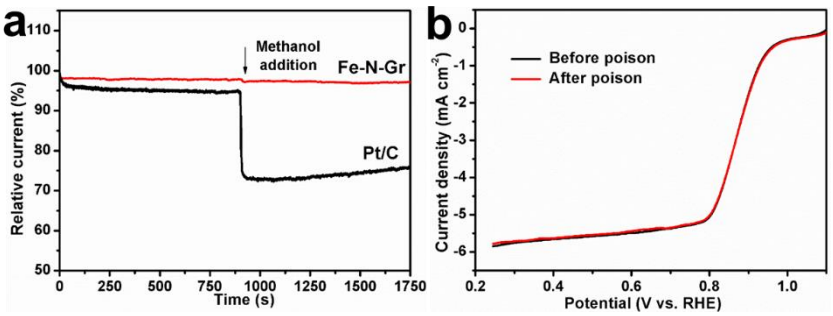

Figure S21. Methanol toxicity test of Fe-N-Gr and commercial Pt/C. (a) Chronoamp erometric response of Fe-N-Gr and Pt/C in O_2-saturated 0.1 M KOH followed by addition of 3 M methanol. (b) LSV curves of Fe-N-Gr before and after poison.

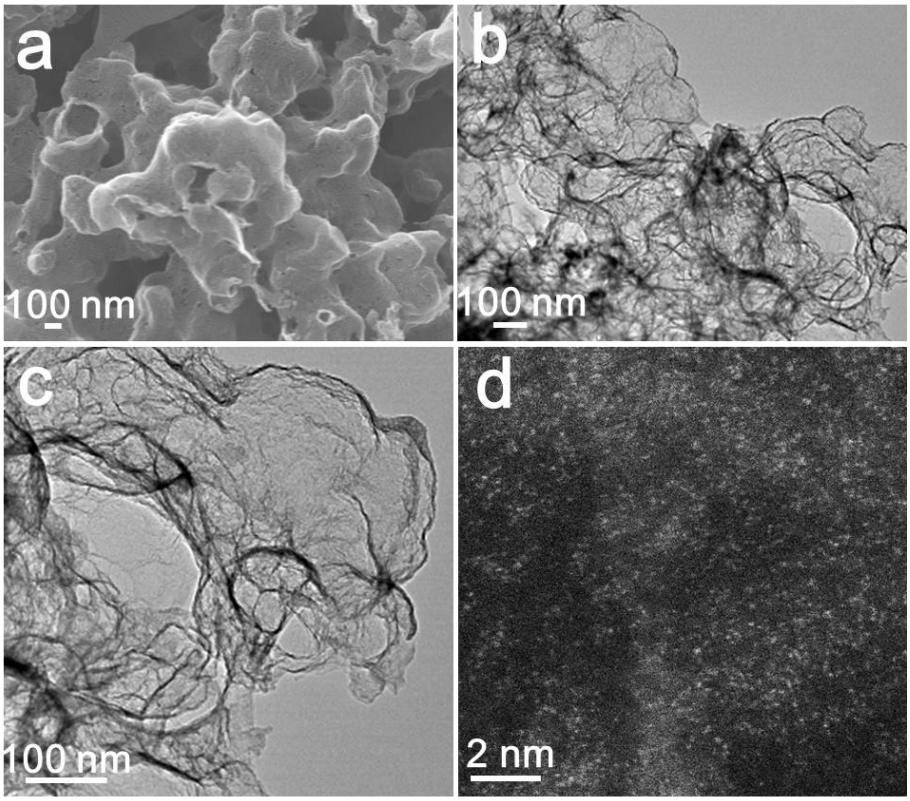

Figure S22. Structural characterizations of the Fe-N-Gr sample after durability tests in O_2-saturated 0.1 M KOH at 1600 rpm and 0.7 V versus RHE. (a) SEM images. (b, c) TEM images. (d) HAADF-STEM image.

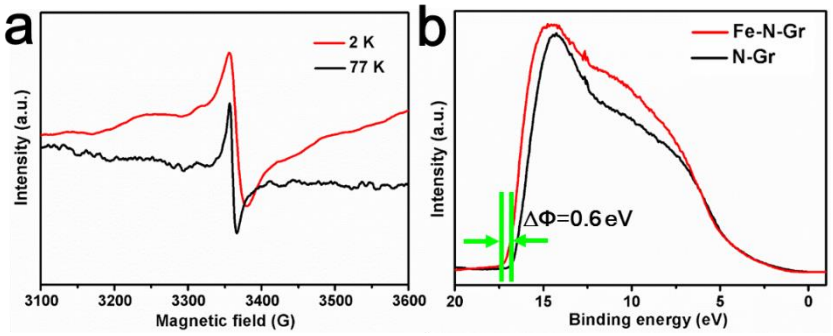

Figure S23. EPR and UPS spectra of the Fe-N-Gr and N-Gr samples. (a) EPR spectra of the Fe-N-Gr catalyst at 77 K and 2 K. (b) UPS spectra of the Fe-N-Gr and N-Gr samples collected using He I (21.2 eV) radiation.

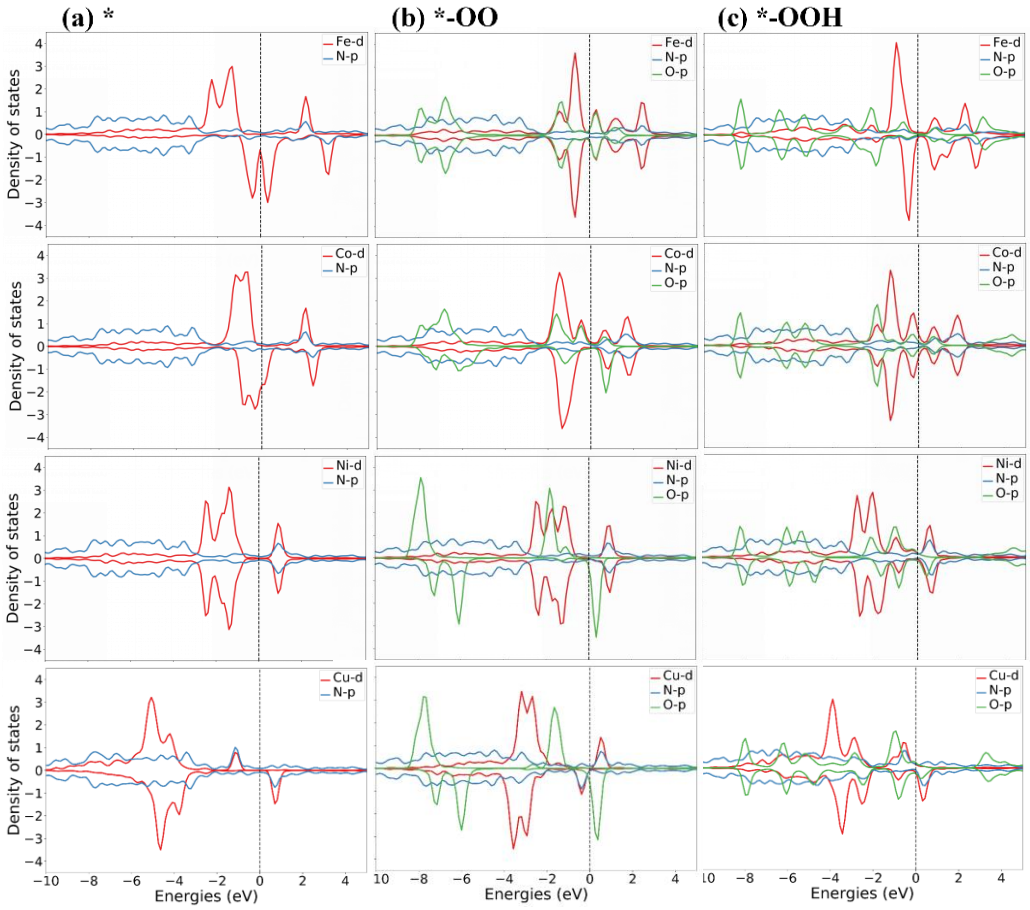

Figure S24. PDOS results of various M-N-Gr samples with ORR intermediates. PDOS results of (a)*, (b)*OO, (c)*OOH for different doping atoms Fe, Co, Ni and Cu in 1st, 2nd, 3rd and 4th rows, respectively. The red, blue and green curves illustrated the PDOS of metal atoms' *d*-orbitals and Oxygen and Nitrogen atoms' *p*-orbitals. The Fermi level located at E = 0 eV.

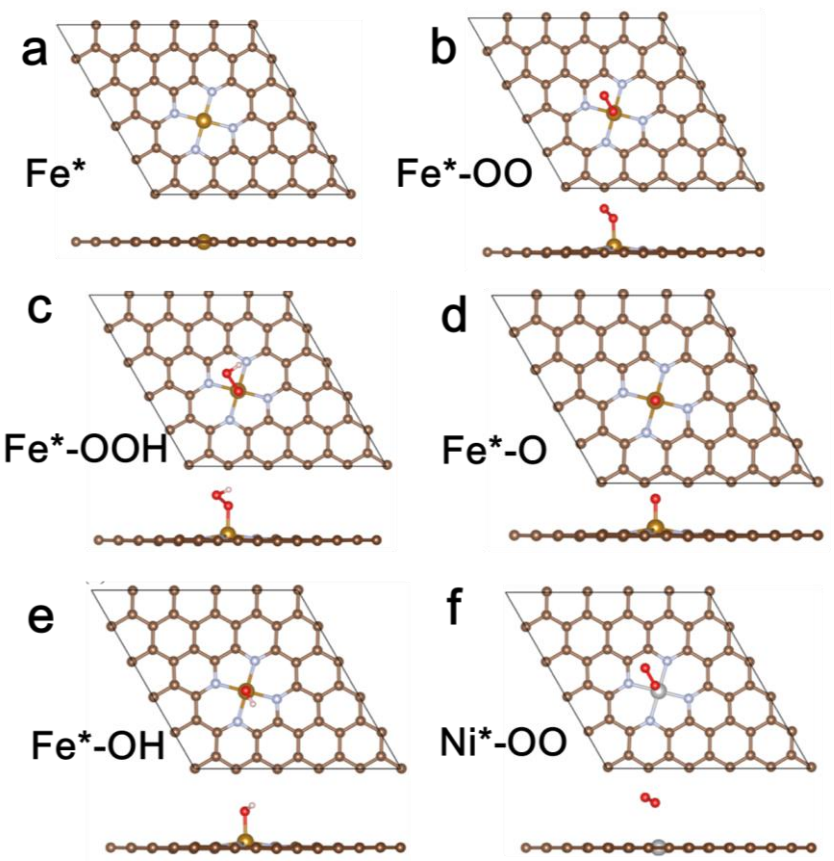

Figure S25. Top and side views of equilibrium Fe-N-Gr and Ni-N-Gr atomic configurations for ORR intermediates. (a) Fe*. (b) Fe*-OO. (c) Fe*-OOH. (d) Fe*-O. (e) Fe*-OH. (f) Ni*-OO, which apparently exhibits physical adsorption of O_2 molecule instead of the chemical bonding in Fe and Co cases.

Supplementary Tables

Table S1. A comparison of the radius of doped ions in ZnO lattices.

Ions	Radius (Å)	Δr
Fe^{2+}	0.78	5.1%
Co^{2+}	0.75	1.3%
Ni^{2+}	0.69	6.7%
Cu^{2+}	0.73	1.3%
Zn^{2+}	0.74	0%

$$\Delta r = \frac{|r1 - r2|}{r1}$$

Here, r1 is the ionic radium of the host material and r2 is the radium of doped ions.

Table S2. EXAFS curve fitting parameters of Co-N-Gr, Fe-N-Gr, Ni-N-Gr and Cu-N-Gr.

Samples	N	R	σ^2 (Å^2)	ΔE_0 (eV)	R-factor
Co-N-Gr	4.0	1.90	0.0055	-7.38	0.0032
Fe-N-Gr	4.1	1.95	0.0073	-1.12	0.0056
Ni-N-Gr	3.8	1.87	0.0027	-2.45	0.0216
Cu-N-Gr	3.1	1.94	0.0052	-1.15	0.0076

Table S3. A comparison of our work and current main synthetic methods for carbon-based SACs.[S13-S21]

Methods	Morphology	Support Precursor	Metal loading	Advantages	Disadvantages	References
Template transformation strategy	**Hollow graphene frameworks**	**Doped ZnO**	**1.2 at% (5.85 wt%)**	**● General synthesis ● Precise control on species and concentration ● Hollow robust framework ● High yield ● Low cost ● Solvent-free ● Relatively high metal loading ● Exposed active sites ● Relatively high conductivity**	**● Template consuming**	**Our work**
Traditional impregnation method	**Graphene sheets**	**Graphene oxide**	**0.05 at% (0.27 wt%)**	**● High conductivity ● Exposed active sites ● General synthesis**	**● Low metal loading ● Easy aggregation ● Solvent consuming**	*Nat. Catal.*, **1**, 63-72 (2018).
Atomic layer loading strategy	**Graphene sheets**	**Graphene sheets**	**2.1 wt%**	**● Precise control ● Uniform metal loading ● Without limited substrates ● Exposed active sites ● Relatively high conductivity**	**● High cost ● Low yield ● Complex manipulation ● Complex equipment**	*J. Am. Chem. Soc.* **137**, 10484-10487 (2015).

Microwave-assisted strategy	**Graphene sheets**	**Graphene oxide**	**1.1 wt%**	**● Simple manipulation ●Rapid synthesis ●General Synthesis ● High conductivity**	**● High temperature ● Solvent consuming ● Low metal loading ● High-cost equipment ● Easy aggregation**	*Adv. Mater.***30**, 1802146 (2018).
Spatial confinement strategy	**Reserved morphologies with precursors**	**Zeolite/ MOFs**	**2.16 wt%**	**● Simple manipulation ● Relatively high metal loading ● Chemical reaction control ● Low cost**	**● Solvent consuming ● Relatively high metal loading ● Unexposed active sites ● Limited metal loadings ● Relatively low conductivity**	*Angew. Chem. Int. Ed.* **56**, 6937-6941 (2017).
Coordination design strategy	**Reserved morphologies with precursors**	**Solid doped MOF crystals**	**4.3 wt%**	**● Simple manipulation ● Relatively high metal loading ● General Synthesis ● Relatively low cost**	**● Solvent consuming ● Relatively high metal loading ● Unexposed active sites ● Relatively low conductivity**	*Angew. Chem. Int. Ed.* **55**, 10800-10805 (2016).
Atom-trapping strategy	**Reserved morphologies with precursors**	**ZIF-8**	**3.76 wt%**	**● Uniform metal loading ● Solvent-Free ● Exposed active sites**	**● High temperature ● High cost ● Complex manipulation**	*Nat. Catal.* **1**, 781-786 (2018).
Photochemical reduction strategy	**Reserved morphologies with precursors**	**Mesoporous carbon**	**2.6 wt%**	**● Uniform metal loading ● Simple manipulation ●Low cost ● Exposed active sites**	**● Limited metal loadings**	*Nat. Commun.* **8**, 1490 (2017).

Table S4. A comparison of ORR catalytic performances in alkaline solution between Fe-N-Gr and other noble-metal-free electrocatalysts reported previously.

Electrocatalysts	Onset potential (V)	$E_{1/2}$ (V)	Electron transfer number	Current density (mA cm^{-2})	References
Fe-N-Gr	1.01	0.87	4.01	6.82	Our work
Fe−N/C-800	0.92	0.81	~3.96	6.06	*J. Am. Chem. Soc.* **136**, 11027-11033 (2014).
Fe-NMCSs	1.02	0.86	4.95	~5.2	*Adv. Mater*. **28**, 7948-7955 (2016).
Co-encapsulated carbon nanotube frameworks	0.97	0.87	3.97	~5.1	*Nat. Energy* **1**, 15006 (2016).
Fe-ISAs/CN	1.00	0.90	3.90	~6.05	*Angew. Chem. Int. Ed.* **56**, 6937-6941 (2017).
Fe-N-CNFs	0.93	0.82	3.93	5.4	*Angew. Chem. Int. Ed.* **54**, 8179-8183 (2015).
Co@MCM	0.95	0.86	3.7	4.55	*Energy Environ. Sci.* **10**, 684-694 (2018).
PANI-Fe-C	0.91	0.81	4.00	3.9	*Science* **332**, 443-447 (2011).
Co-NC	0.90	0.83	3.72	~4.5	*Angew. Chem. Int. Ed.* **55**, 4087-4091 (2016).
FeSAs/PTF-600	1.01	0.87	3.88	5.51	*ACS Energy Lett.* **3**, 883-889 (2018).
IAG-C	1.03	0.86	~3.95	6.32	*Sci. Adv.* **1**, e1400035 (2015).

Table S5. DFT total energies (*E*) of ORR intermediates with different dopants.

Intermediates	Fe (eV)	Co (eV)	Ni (eV)	Cu (eV)
***OOH**	-462.757	-461.298	-459.179	-456.344
***OO**	-458.570	-457.324	-455.447	-452.436
***OH**	-458.230	-456.780	-454.573	-451.736
***O**	-453.778	-451.518	-448.939	-446.007
*****	-447.621	-446.648	-445.369	-442.433

Table S6. Zero point energies (*ZPE*), and entropy contribution (*TS*) of ORR intermediates.

Intermediates	ZPE (ev)	TS (eV)
***OOH**	0.45	0.15
***OO**	0.16	0.12
***OH**	0.37	0.07
***O**	0.08	0.05
*****	0	0

Table S7. The equilibrium metal-oxygen binding distances for different dopants.

Intermediates	Fe (Å)	Co (Å)	Ni (Å)	Cu (Å)
*-OO	1.75	1.89	2.71	2.65
*-OOH	1.78	1.88	2.13	1.79
*-O	1.66	1.71	1.72	1.86
*-OH	1.82	1.87	2.00	1.96

References

S1. Kresse, G. & Furthmüller, J. Efficient iterative schemes for ab initio total-energy calculations using a plane-wave basis set. *Phys. Rev. B* **1996**, *54*, 11169.

S2. Perdew, J.P., Burke, K. & Ernzerhof, M. Generalized gradient approximation made simple. *Phys. Rev. Lett.* **1996**, *77*, 3865-3868.

S3. Blöchl, P.E. Projector augmented-wave method. *Phys. Rev. B* **1994**, *50*, 17953-17979.

S4. Kresse, G. & Joubert, D. From ultrasoft pseudopotentials to the projector augmented-wave method. *Phys. Rev. B* **1999**, *59*, 1758-1775.

S5. Grimme, S., Antony, J., Ehrlich, S. & Krieg, H. A consistent and accurate ab initio parametrization of density functional dispersion correction (DFT-D) for the 94 elements H-Pu. *J. Chem. Phys.* **2010**, *132*, 154104.

S6. Xu, H., Cheng, D., Cao, D. & Zeng, X.C. A universal principle for a rational design of single-atom electrocatalysts. *Nat. Catal.* **2018**, *1*, 339-348.

S7. Rogers, G.W. & Liu, J.Z. Graphene actuators: quantum-mechanical and electrostatic double-layer effects. *J. Am. Chem. Soc.* **2011**, *133*, 10858-10863.

S8. Mann, G.W. et al. First-principles Hubbard U approach for small molecule binding in metal-organic frameworks. *J. Chem. Phys.* **2016**, *144*, 174104.

S9. Wang, L., Maxisch, T. & Ceder, G. Oxidation energies of transition metal oxides within the GGA+U framework. *Phys. Rev. B* **2006**, *73*, 195107.

S10. Chen, Y. et al. Isolated single iron atoms anchored on N-doped porous carbon as an efficient electrocatalyst for the oxygen reduction reaction. *Angew. Chem. Int. Ed.* **2017**, *56*, 6937-6941.

S11. Jiao, Y., Zheng, Y., Jaroniec, M. & Qiao, S.Z. Design of electrocatalysts for oxygen- and hydrogen-involving energy conversion reactions. *Chem. Soc. Rev.* **2015**, *44*, 2060-2086.

S12. Nørskov, J.K. et al. Origin of the overpotential for oxygen reduction at a fuel-cell cathode. *J. Phys. Chem. B* **2004**, *108*, 17886-17892.

S13. Fei, H. et al. General synthesis and definitive structural identification of MN_4C_4 single-atom catalysts with tunable electrocatalytic activities. *Nat. Catal.* **2018**, *1*, 63-72.

S14. Yan, H. et al. Single-atom Pd_1/graphene catalyst achieved by atomic layer deposition: Remarkable performance in selective hydrogenation of 1,3-butadiene. *J. Am. Chem. Soc.* **2015**, *137*, 10484-10487.

S15. Yin, P. et al. Single cobalt atoms with precise N-coordination as superior oxygen reduction reaction catalysts. *Angew. Chem. Int. Ed.* **2016**, *55*, 10800-10805.

S16. Jones, J. et al. Thermally stable single-atom platinum-on-ceria catalysts via atom trapping. *Science* **2016**, *353*, 150-154.

S17. Wei, H. et al. Iced photochemical reduction to synthesize atomically dispersed metals by suppressing nanocrystal growth. *Nat. Commun.* **2017**, *8*, 1490.

S18. Xia, B.Y. et al. A metal-organic framework-derived bifunctional oxygen electrocatalyst. *Nat. Energy* **2016**, *1*, 15006.

S19. Chen, Y. et al. Isolated single iron atoms anchored on N-doped porous carbon as an efficient electrocatalyst for the oxygen reduction reaction. *Angew. Chem. Int. Ed.* **2017**, *56*, 6937-6941.
S20. Yi, J.-D. et al. Atomically dispersed iron-nitrogen active sites within porphyrinic triazine-based frameworks for oxygen reduction reaction in both alkaline and acidic media. *ACS Energy Lett.* **2018**, *3*, 883-889.
S21. Wang, Z.L. et al. Gelatin-derived sustainable carbon-based functional materials for energy conversion and storage with controllability of structure and component. *Sci. Adv.* **2015**, *1*, e1400035.